Research Article | Vol. 30, No. 8 / 11 Apr 2022 / Optics Express 13184
Optics EXPRESS

Slow saturable absorption for optimal operation in a soliton comb laser

ZHE KANG,[1,4,7] YINGHE WANG,[2,7] SHAOKANG WANG,[3,*] ZI-WEI ZHENG,[5] XIANTING ZHANG,[6] AND CURTIS R. MENYUK[3]

[1]*Ningbo Research Institute, Zhejiang University, Ningbo 315100, China*
[2]*School of Electronic and Information Engineering, Shanghai Dianji University, Shanghai 201306, China*
[3]*Department of Computer Science and Electrical Engineering, University of Maryland, Baltimore County, 1000 Hilltop Circle, Baltimore, MD 21250, USA*
[4]*Centre for Optical and Electromagnetic Research, College of Optical Science and Engineering, National Engineering Research Center for Optical Instruments, Zhejiang University, Hangzhou 310058, China*
[5]*Digital Industry Research Institute, Zhejiang Wanli University, Ningbo 315100, China*
[6]*Department of Electronic and Information Engineering, The Hong Kong Polytechnic University, Hung Hom, Kowloon, Hong Kong, China*
[7]*Contributed equally*
[*]*swan1@umbc.edu*

Abstract: In this article, we study how the choice of parameters of a slow saturable absorber (SSA) affects the stable operation of a soliton fiber comb laser. We show that a shorter recovery time for the SSA does not always lead to shorter modelocked pulses. Instead, increasing the cavity gain plays a critical role in generating stable modelocked pulses with higher energy and shorter durations. We find that more stable, shorter, and more energetic output pulses can be achieved with lower saturation energies of the SSA and/or higher anomalous dispersion within the cavity.

1. Introduction

In recent years, optical frequency combs have become widely used in both research and the industry and in both military and civil fields [1–6]. A sizable fraction of current frequency comb sources are based on passively modelocked fiber lasers [7–13]. Among such modelocked lasers, millimeter-scale semiconductor saturable absorber mirrors (SESAMs) are widely used as a key intracavity component to achieve stable operation [8,13–16]. To design modelocked lasers and comb sources for particular applications, the selection of a proper SESAM is vital. The SESAM parameters such as the saturation fluence, the recovery time, as well as the unsaturated loss (or the flat loss) must be carefully specified to obtain the optimal output from the laser cavity. In particular, it is useful to understand where in the system parameter space stable stationary pulse solutions exist, and how the pulse profile changes as parameters change.

SESAMs are slow saturable absorbers (SSA), in which "slow" implies a recovery time T_A that is longer than the optical pulse duration in the frequency comb source. The typical absorption recovery time of a GaAs-based SESAM is usually between 0.5 ps and 30 ps [17–19], which is considerably longer than the duration of the generated modelocked pulse (~100s fs), although shorter than the round trip times (~10 ns). Other bulk-structured materials that have similar slow absorption recovery times include carbon nanotubes [20–22], graphene [23], and few-layer molybdenum diselenide [24]. Currently, the recovery time of bulk-structured saturable absorbers ranges from 0.1 ps to hundreds of picoseconds [25].

Multiple studies have described the dependence of the stationary modelocked pulse profile as the energy balance varies in modelocked lasers using slow saturable absorbers. Paschotta and Keller [26] derived an analytical estimate of the pulse duration using the SSA's absorption

#454207 https://doi.org/10.1364/OE.454207
Journal © 2022 Received 25 Jan 2022; revised 23 Mar 2022; accepted 25 Mar 2022; published 5 Apr 2022

Optics EXPRESS

depth and saturation energy. In addition, they found that the pulses become unstable when the recovery time becomes sufficiently large. In a later study, it was demonstrated that the stable pulse profiles are consistent with the soliton area theorem [27]. Kärtner, *et. al* [28] showed that as the small-signal gain increases, the pulse profiles become similar to the profiles of the modelocked pulses that are generated by lasers that use a fast saturable absorber, while the pulse duration and time-bandwidth product remains almost unchanged. However, there has not been a careful study of the effect that the SSA's recovery time and saturation energy have on the profile of the output pulses.

Fast saturable absorbers (FSAs), like those based on nonlinear polarization rotation (NPR) [9–11], are a commonly used alternative to SSAs. These saturable absorbers, which rely on interferemetric effects on the scale of the optical wavelength and the Kerr effect, are effectively instantaneous. While maintaining interferemetric stability is challenging, these lasers are remarkably stable when that can be accomplished. Hence, there exists a popular assumption [26,29,30] that SSAs with shorter recovery times will produce shorter modelocked pulses and thus broader bandwidth output combs. However, using the evolutionary simulation method [31–33], Lee *et al.* recently showed that the pulse duration and thus the bandwidth remain almost unchanged for soliton lasers as the recovery time decreases [25]. Lee *et al.*'s results appear to contradict the notion that a shorter recovery time is always preferred, and this assumption requires a closer look. More generally, it is important for the design and optimization of future SSA-based soliton lasers to provide a more thorough description of where in the experimentally-adjustable parameter space stable pulses exist and to determine the variation of their profiles within the stable parameter regions.

Using a SESAM-based fiber comb laser as an example, we show in detail how changing the recovery time T_A affects the region of stable operation. We stress that our goal is not to carry out a quantitative performance comparison between an FSA and an SSA. Such a comparison would not only be difficult, but it would also be unfair because of the fundamental difference in their physics, as we will show in Sec. 3. In this article, our goal is to provide general guidance for selecting an SSA for soliton comb lasers. We achieve this goal by studying the regions of stable modelocking operation for the SSA parameters. We show that although the SESAM's absorption recovers faster as T_A decrease, which helps to stabilize modelocking, the absorption also significantly weakens, which works against stable modelocking. Hence, the long-held assumption [26,29,30] that a lower T_A is always preferred should be revised. Plus, careful parameter selection for the SSA is needed for optimal modelocking performance. We then find that in order to obtain more energetic and broadband stable modelocked pulses, the key is to achieve larger cavity gain. In order to maximize the cavity gain, the SESAM's recovery time T_A must be carefully selected to be around 0.5 ps. We also find that the modelocked pulse profile can be further optimized by using lower values of the SESAM saturation energy and larger negative group delay dispersion.

In Sec. 2, we present the computational model that we use for conducting our parameter studies. In Sec. 3, we show the fundamental dynamical structure of the SESAM-based modelocking system in terms of the SESAM recovery time T_A, as well as the unsaturated cavity gain g_0. We also obtain an optimal output pulse when the recovery time $T_A = 0.43$ ps, which is close to the limit of commercially available SESAMs at this time. In Sec. 4, we further show that a lower saturation energy of the SESAM and/or a larger anomalous dispersion can help stabilize the modelocking and thus enable the generation of more energetic and larger bandwidth output combs. We conclude this work in Sec. 5.

2. SESAM-based soliton fiber comb laser

Our study is based on a reported highly stable fiber comb laser with a repetition frequency of 200 MHz [8]. We use an averaged model [34,35] and dynamical methods [36] to carry out the parameter study. The averaged model [35,37] that we use is a variant of the Haus modelocking

Optics EXPRESS

equation [38]. The evolution of the wave envelope is described by

$$T_R\frac{\partial u}{\partial T} = -i\phi u + t_s\frac{\partial u}{\partial t} + \frac{g(|u|)}{2}\left(1 + \frac{1}{2\omega_g^2}\frac{\partial^2}{\partial t^2}\right)u - \frac{l}{2}u - i\frac{\beta''}{2}\frac{\partial^2 u}{\partial t^2} + i\gamma\,|u|^2\,u - \frac{\rho}{2}f_{\mathrm{sa}}(t)u, \quad (1)$$

where T_R is the round trip time, T is the slow time of propagation, t is the retarded fast time, $u(t, T)$ is the slowly varying field envelope, and each operator on u on the right-hand side of Eq. (1) is averaged over one round trip. The time t_s is the time shift in the fast time t of the pulse centroid

$$t_s = \int_{-T_R/2}^{T_R/2} t'\,|u(t')|^2\,\mathrm{d}t' \Big/ \int_{-T_R/2}^{T_R/2} |u(t')|^2\,\mathrm{d}t', \quad (2)$$

the variable ϕ is the phase change, $g(|u|)$ is the saturated gain, ω_g is the gain bandwidth, l is the linear loss in the cavity, β'' is the group-delay dispersion, γ is the Kerr coefficient, ρ is the saturable absorption coefficient, and $f_{\mathrm{sa}}(t)$ is the saturable absorption function. We assume that the recovery time of the gain is significantly longer than the round trip time, so that the gain $g(|u|)$ may be written as

$$g(|u|) = g_0/[1 + w(|u|)/(P_{\mathrm{sat}}T_R)]\,, \quad (3)$$

where g_0 is the unsaturated gain, $w(|u|)$ is the intra-cavity pulse energy,

$$w(|u|) = \int_{-T_R/2}^{T_R/2} |u(t)|^2\,\mathrm{d}t, \quad (4)$$

and P_{sat} is the saturation power of the doped fiber. Here, we model $f_{\mathrm{sa}}(t)$ using a two-level slow saturable absorption model

$$f_{\mathrm{sa}}(t) = n(t), \qquad \frac{\mathrm{d}n(t)}{\mathrm{d}t} = \frac{1-n}{T_A} - \frac{|u(t)|^2}{w_A}n, \qquad n\left(-\frac{T_R}{2}\right) = 1, \quad (5)$$

where n is the ratio of the lower level population to the total population of the SESAM [37], w_A is the saturation energy of the SESAM, and we assume that the response time $T_A \ll T_R$.

The parameters that we use are listed Table 1. The variable l corresponds to a total cavity loss of 22%, which includes both the output coupling ratio and the insertion losses among the cavity components. The saturable coefficient ρ corresponds to a SESAM modulation depth of about 10%. From the reported saturation fluence Φ_{sat} and the effective area $A_{\mathrm{eff,SESAM}}$, the saturation energy is $w_A = \Phi_{\mathrm{sat}}A_{\mathrm{eff,SESAM}} = 50\,\mu\mathrm{J/cm^2} \times 314\mu\mathrm{m^2} = 157\,\mathrm{pJ}$ [19] (Here, we correct the units of Φ_{sat} and $A_{\mathrm{eff,SESAM}}$ on page 2363 in [35]).

Table 1. Value of parameters we use in Eq. (1).

Parameter	Value	Parameter	Value
T_R	5.00 ns	P_{sat}	0.744 mW
β''	-0.01 ps^2	w_A	157 pJ
ω_g	16.54 ps^{-2}	γ	1.59 kW^{-1}
l	0.25	T_A	2.00 ps
ρ	0.11		

In Fig. 1, we show the change in normalized absorption $n(t)$ of the SESAM as T_A and w_A vary, in which $n(t) = 1$ indicates that the absorption is unsaturated. The incoming pulse profile is chosen to be similar to that of the experimental pulse in [8]. In general, we observe that the absorption $n(t)$ decreases as the incoming pulse appears, and recovers gradually to the unsaturated

Optics EXPRESS

level, $n(t) = 1$, in the wake of the pulse. By comparison, in Fig. 1, we also show the profile of a fast saturable absorber (FSA) based on the equation

$$f_{\text{sa}}(t) = \frac{1}{1 + |u(t)|^2 / P_{\text{sat}}}, \tag{6}$$

where P_{sat} is the saturation power [39]. Here, we set $P_{\text{sat}} = w_A/T_R$, where $w_A = 157\,\text{pJ}$, to be convenient for illustrations. In practice, w_A is an SSA parameter and has no connection to the FSA parameter P_{sat}.

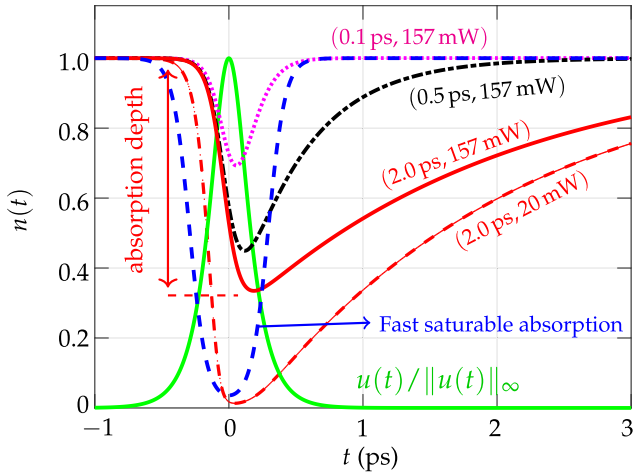

Fig. 1. The variation of the normalized absorption of the SESAM when varying (T_A, w_A) — values are shown next to the corresponding lines. Here, the incoming pulse is given by $u(t) = \sqrt{U_0/(2\tau)}\,\text{sech}(t/\tau)$, where $U_0 = 211\,\text{pJ}$ and $\tau = 125\,\text{fs}$.

In Fig. 1, we show that as T_A decreases, with $w_A = 157\,\text{pJ}$, the absorption recovery of the SESAM occurs more quickly. Hence, the SESAM recovers more quickly, which can potentially help stabilize the modelocked pulse by suppressing the wake modes trailing the modelocked pulse [35]. This operating regime was described in [25]. However, as we show in Fig. 1, when T_A decreases while w_A is fixed at 157 mW, the SESAM's absorption depth $n(t)$ decreases significantly at the same time, and thus increasingly deviates from the behavior of an FSA, which we also show in Fig. 1. Unsurprisingly, we will later show that the decrease in SESAM's absorption depth works against stable modelocking. This result is unsurprising because in the limit as $T_A \to 0$, the SESAM effectively disappears. This behavior is remarkably different from FSAs [39,40], which have large parameter regions in which modelocked operation is stable and the output modelocked pulse energy is only limited by the instability of continuous waves [41]. In Sec. 3, we will also show that the stability of the SESAM-based laser is also limited by continuous waves when T_A becomes sufficiently small, but this limit is less important than in the FSA-based laser because the absorption depth in this limit is already small. In Fig. 1, we also show the case $T_A = 2.0\,\text{ps}, w_A = 20\,\text{pJ}$. Comparing with the case $T_A = 2.0\,\text{ps}, w_A = 157\,\text{pJ}$, we observe that the absorption depth visibly increases and becomes more comparable to the absorption depth of the FSA. Thus, in order to approximate the operation of an FSA and produce more broadband and energetic modelocked pulses, one would need to reducing both T_A and w_A simultaneously. Hence, careful selection of the SSA parameters is necessary to achieve optimal performance. In Sec. 3, we will explicitly calculate the impact of changing T_A on the SESAM-based laser's stable operating region and in Sec. 4, we will do the same for w_A.

Optics EXPRESS

Despite the comparison that we show in Fig. 1, we do not directly compare the absorption depth and the subsequent modelocking performance of an FSA and an SSA, as it would not be very meaningful to do so. An SSA is typically a single device so that its saturation energy is well-defined and easily quantifiable. By contrast, an FSA is typically realized by combining several optical components. So, for example, a common FSA will combine nonlinear polarization rotation in a nonlinear fiber with polarization-selection elements [42]. As a consequence, the saturation power P_{sat} is usually a heuristic quantity and thus very difficult to quantify. Moreover, with either an FSA or an SSA, we cannot set the absorption depth *a priori*. It is a parameter that depends on the energy of the modelocked pulse and must be determined *a posteriori*.

3. Optimizating the SESAM recovery time

We first determine the stability of modelocked pulses using the dynamical method [34,36]. This method is a set of computational algorithms that make it possible to determine the precise region in the experimentally-adjustable parameter space where stable pulse solutions exist. A modelocked laser can be viewed as a nonlinear dynamical system, and a modelocked pulse $u_0(t)$ can be viewed as a stationary solution or an equilibrium of such a system. In the dynamical method, we find the stationary solution u_0, the linear phase rotation coefficient ϕ, and the time shift t_s using Newton's method. The computational root-finding procedure is described in detail in [36]. If any possible perturbation $\Delta u(t, T)$ of the stationary pulse $u_0(t, T)$ grows exponentially, then the modelocked pulse is unstable. The stability can be determined by solving a linear eigenvalue problem

$$\mathsf{L}\mathbf{e}_k = \lambda_k \mathbf{e}_k, \tag{7}$$

where the matrix L can be written as

$$\mathsf{L} = \begin{bmatrix} \mathsf{L}_{11}(u), & \mathsf{L}_{12}(u) \\ \mathsf{L}_{21}(u), & \mathsf{L}_{22}(u) \end{bmatrix}\Bigg|_{u=u_0}, \tag{8}$$

in which $\mathsf{L}_{11} = \delta\mathcal{F}/\delta u$, $\mathsf{L}_{12} = \delta\mathcal{F}/\delta u^*$, $\mathsf{L}_{21} = \delta\mathcal{F}^*/\delta u$, $\mathsf{L}_{22} = \delta\mathcal{F}^*/\delta u^*$ are functional derivatives [34,43], $\mathcal{F}(u)$ is defined by the right-hand side of Eq. (1), and λ_k and $\mathbf{e}_k$ are the kth eigenvalue and eigenfunction of the matrix L. Any perturbation $\Delta u(t, T)$ can be expressed as a linear combination of the eigenvectors $\mathbf{e}_k$. A stable modelocked pulse u_0 exists only when all the λ_k have non-positive real parts.

The dynamical method allows us to determine the existence and stability of pulses over a broad parameter range efficiently and unambiguously. By contrast, when using traditional evolutionary methods—for example, the popular split-step method [31–33]—it is often uncertain how long it takes for the system to evolve into a stable profile, especially when the system is approaching a stability boundary. Additionally, if multiple stable profiles exist, the final evolution profile would depend on the initial conditions that are chosen. These ambiguities are typically difficult to resolve when using evolutionary methods.

In Fig. 2, we show the stable regions in the parameter space of the unsaturated gain g_0 and the SESAM recovery time T_A. For any given pair T_A and g_0, we calculate the stationary modelocked pulse solution u_0 and evaluate the dynamical spectrum, which we show later in Fig. 3. When T_A becomes sufficiently small, we discover a continuous region of stable operation (the white-shaded area) that is enclosed by three different boundaries: a lower bound and an upper bound in g_0 due to unstable continuous waves (C_s) and an upper bound in g_0, S_s, due to unstable soliton wake modes.

As shown in Fig. 2, when $T_A = 2$ ps, which is the value for a typical SESAM [44] that is used in fiber comb lasers, stable modelocked pulses exists when $0.57 < g_0 < 7.0$. The continuous waves become unstable when $g_0 < 0.57$ (indicated by the curve C_s) while the wake modes become

Optics EXPRESS

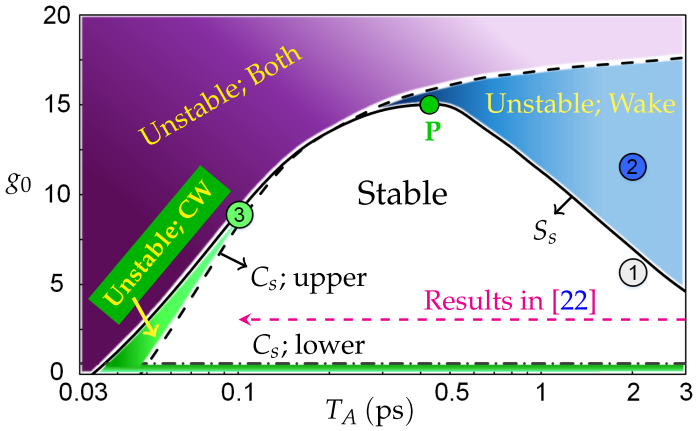

Fig. 2. Stability map in (T_A, g_0) space. The symbols C_s and S_s represent the stability boundaries due to the continuous waves (CW) and the wake modes, respectively.

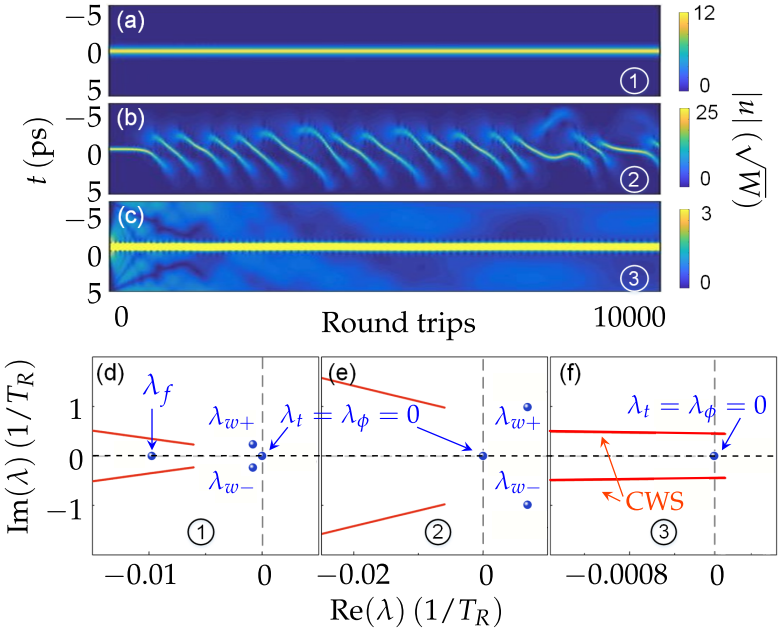

Fig. 3. (a)(b)(c) The temporal evolution profiles of points ①–③ in Fig. 2. Here, the initial conditions are a one-photon-per-mode noise seed. We obtained similar stable/unstable propagation profiles when using pulsed initial conditions. These results suggest that the system does not support multiple stable solutions using the selected sets of system parameters. (d)(e)(f) The dynamical spectra of these points; In all three subplots, the eigenvalue λ_a is too negative to be shown in the plotted area. We use "CWS" in (f) to represent the continuous waves spectra, which also appear as the orange lines in (d) and (e).

Optics EXPRESS

unstable when g_0>7.0 (indicated by the curve S_s). As an example, at point ①, where $T_A = 2$ ps and $g_0 = 6.0$, the system supports a stable modelocked pulse. We show the corresponding evolution profile in Fig. 3(a), and the dynamical spectrum in Fig. 3(d). We observe in the dynamical spectra that there are two continuous branches of continuous waves eigenvalues, and four discrete eigenvalues on the real axis, λ_a, λ_ϕ, λ_t, and λ_f that correspond to the perturbations to the amplitude, phase, central time, and central frequency, as suggested by soliton perturabtion theory [45–47]. Additionally, there are a pair of complex conjugate eigenvalues λ_{w+} and λ_{w-} that correspond to the soliton wake modes [34,35]. All eigenvalues have non-negative real parts, which confirms that the stationary modelocked pulse is stable, as suggested by Fig. 3(a). By contrast, at point ②, at which $T_A = 2$ ps and $g_0 = 12.0$, the stationary pulse is unstable due to the wake modes. The corresponding evolution profile is shown in Figs. 3(b), in which we observe the subsequent construction and destruction of new pulses. The dynamical spectra in Figs. 3(e) show that $\mathrm{Re}(\lambda_{w+,w-})>0$, which indicates that the wakes modes are unstable. These results agree well with prior results [35].

Starting from $T_A = 3$ ps, we observe that the stable region first expands as T_A decreases, and then shrinks when T_A decreases below 0.43 ps. The stable region ultimately disappears when $T_A \leq 0.05$ ps. By comparison, when T_A>3 ps, we observe a similar stability structure as when $T_A = 3$ ps and the stable region continues to exist up to $T_A = 7$ ps. We did not study larger values of T_A as they are of little practical interest for frequency comb applications.

In Fig. 2, we observe that when g_0 becomes sufficiently large, a stable modelocked pulse is destablized by different mechanisms that depend on T_A:

- When T_A>0.18 ps, a stable modelocked pulse is destabilized by the wake modes, while the continuous waves remain stable, as shown by the blue region (above line S_s) in Fig. 2. This case was discussed in detail in [35] which includes a cartoon of the pulse evolution.
- By contrast, when T_A<0.18 ps, the modelocked pulse is destabilized by continuous waves while the wake modes are stable, as shown by the green triangular region (above line C_s, upper) in Fig. 2. Prior studies showed that continuous waves destabilize modelocked FSA-based lasers as cavity gain grows [41]. This result is consistent with ours, as the SESAM behaves similarly to an FSA with decreasing absorption depth as T_A decreases, as suggested in Fig. 1.
- Although we can still computationally find stationary solutions as $T_A \to 0$, these solutions become unstable because the saturable absorption disappears, as shown in Fig. 1.

In Fig. 3, we show an examples in which $g_0 = 8.5$ and $T_A = 0.1$ ps and continuous waves are unstable. We show the unstable evolution profile in Fig. 3(c), in which we observe that the continuous waves continues to fluctuate around the propagating pulse. In addition, the pulse amplitude experiences quasi-periodic modulations due to its interference with the unstable continuous waves. The corresponding spectrum in Fig. 3(f), in which we observe that parts of the two branches of the continous spectrum have positive real parts, consistent with [35,36]. Both the wake modes and the continous waves are unstable in the purple region above both lines (C_s, upper) and S_s, as shown in Fig. 2.

In Fig. 4, we show the variation of the stable modelocked pulses inside the stable region that we show in Fig. 2. Here, we can confirm that the profile of the calculated stable modelocked pulses largely agree with the soliton area theorem [28,48]

$$E_0 t_0 = 2\,|\beta''|\,/\gamma = 12.6\,(\mathrm{W}\cdot\mathrm{ps}^2), \tag{9}$$

where $E_0 = \int_{-T_R/2}^{T_R/2} |u_0|^2\,\mathrm{d}t$ is the pulse energy, and $t_0 = \mathrm{FWHM}/1.763$ in which FWHM is the full-width-half-maximum pulse duration. This energy theorem has significant implications for

Optics EXPRESS

practical laser designs. An important design goal for comb lasers is to increase the output comb power/energy as well as the bandwidth. Here, Eq. (9) indicates that for SESAM-based soliton fiber comb lasers, a growth in pulse energy is conveniently accompanied by decrease in pulse duration and thus broader bandwidth. In Fig. 4(b), we also observe that for a given T_A, the pulse duration decreases, while the pulse energy E_0 increases almost linearly when we increase the unsaturated gain g_0. By comparison, as shown in Fig. 4(a), both the pulse duration and the energy remain almost unchanged as T_A decreases when g_0 is fixed, which is consistent with [25].

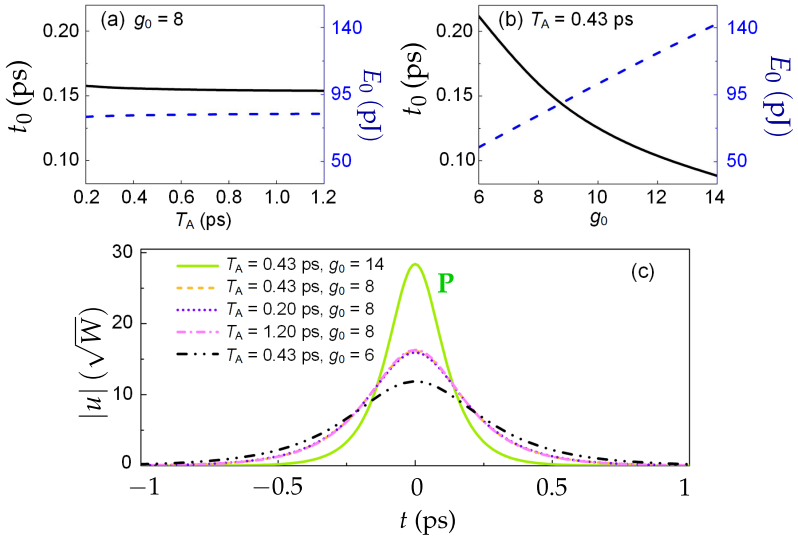

Fig. 4. (a)(b): the variation of the calculated pulse duration t_0 and the soliton area $E_0\tau_0$ in the (g_0, T_A) space as shown in Fig. 2. (c): the correponding pulse profile of a few selected points in (a) and (b).

Thus, this observation provides an unambiguous answer to the question that was posed at the beginning: A shorter recovery time of the SSA does *not* necessarily lead to a shorter modelocked pulse. Instead, a higher cavity gain leads to a higher pulse energy and a wider pulse bandwidth. Therefore, to optimize the laser's output profile, one should find a recovery time that can allow the highest unsaturated gain for stable modelocking.

For our parameters, we find that by selecting a SESAM with $T_A = 0.43$ ps, we obtain the largest cavity gain $g_0 = 14$, which corresponds to a small signal gain of 61 dB. In Fig. 2, we label this optimal point as **P**. In Fig. 4(c), we show the stable pulse profile at **P**, as well as a few other points for comparison. We observe that when $T_A = 0.43$ ps, increasing g_0 from 6 to 14 leads to a growth of pulse energy from 59.6 pJ to 142.7 pJ. Simultaneously, the pulse duration decreases from 212 fs to 88 fs.

4. Further improvements in output energy and bandwidth

Next, we show how the system improves as the SSA's saturable energy w_A and the cavity GDD β'' vary.

In Sec. 3, we showed that the change in the system's dynamical spectrum and the output pulse's profile as the SSA's recovery time T_A varies. In Fig. 2, we show that for a given w_A, we can find an upper bound which is a composite curve of (C_s, upper) and S_s. We then show the optimal pulse profile at **P** in Fig. 4. In Fig. 5, we show the change of the upper stability boundary and the corresponding pulse profiles as the saturation energy w_A changes. In Fig. 5(a), we find that the stability boundary (S_s, upper) moves to larger values of g_0 as w_A decreases. This result

Optics EXPRESS

suggests that by lowering the SESAM saturation power, the laser cavity can operate stably with higher gains, leading to more energetic modelocked pulses with a larger bandwidth. We then show the change of the largest unsaturated gain, g_0, consistent with pulse stability as well as the corresponding pulse profiles in subplots (b) and (c). Starting from the optimal point **P** in Fig. 2, we observe that the largest possible gain g_0 grows almost linearly as w_A decreases, as shown in Fig. 5(b). We take four points along the line of $T_A = 0.43$ ps, marked as points {1}, {2}, {3}, and {4} in Fig. 5(b), and show the corresponding pulse profile in Fig. 5(3). In Fig. 5(c), we observe that as w_A decreases and g_0 increases, the stable modelocked pulse continues to become narrower and more energetic. When w_A is 20 pJ, the corresponding pulse energy is 238.5 pJ, while the pulse duration is 52.7 fs, which is a 67% increase in pulse energy and a 40% decrease in pulse duration.

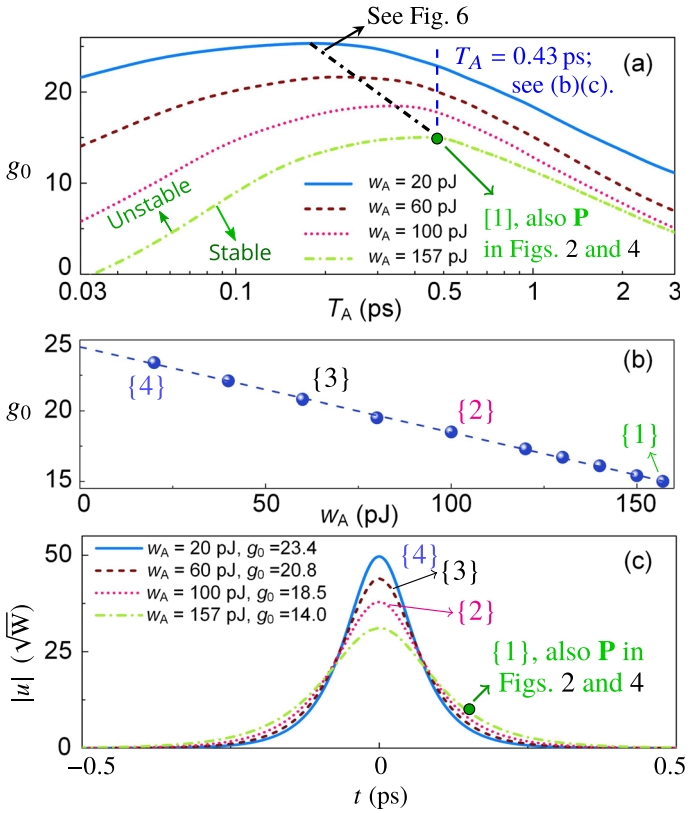

Fig. 5. (a) The stability boundary as the saturation energy w_A varies. For each value of w_A, the region below the line indicates where stable modelocked pulses exist. We show several cases when $T_A = 0.43$ ps: (b) The largest g_0 that is consistent with stable modelocking as the SESAM's saturation energy w_A varies. (c) The pulse profiles corresponding to the marked points in (b).

In Fig. 6, based on the data in Fig. 5, we show how the optimal value of the SSA's recovery time T_A varies as the saturation energy w_A changes. In the range of parameters that we study, we observe that as w_A decreases, the optimal value of T_A appears to decrease linearly. This observation will be useful for experimentalists to improve their laser designs. In the future, we expect to study the variation of the optimal T_A for a wider range of w_A, as well as when other system parameters vary.

Optics EXPRESS

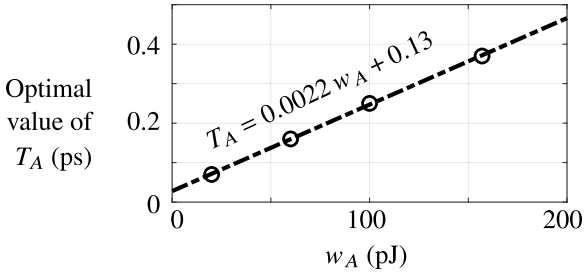

Fig. 6. The location of the optimal T_A as the saturable energy w_A varies when $\beta'' = -0.01$ ps^2. The black dash-dotted line, which shows a linear trend between w_A and the optimal T_A, is fitted using the optimal values that are obtained when $w_A = 20$ pJ, 60 pJ, 100 pJ, and 157 pJ, shown in Fig. 5(a).

Another approach to further increase the output energy and bandwidth is to introduce more negative dispersion. In Fig. 7, we show the upper stability bounds in g_0 as we vary the group delay dispersion (GDD) β'' while keeping other system parameters fixed. We see that the basic structure is the same as in Fig. 2. When β'' becomes more negative, both lines (C_s, upper) and S_s, as well as the location of the optimal point **P**, shift to lower values of T_A and larger values of g_0.

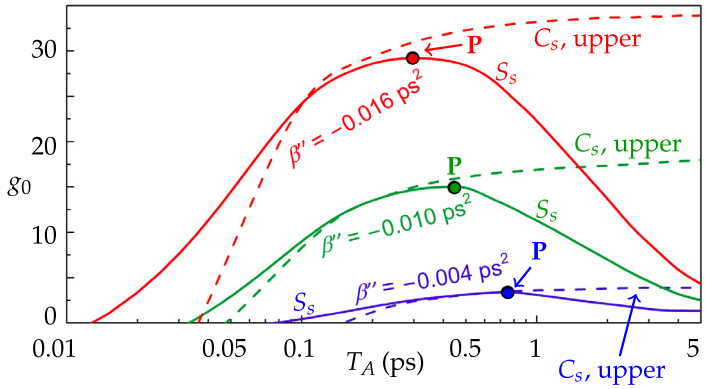

Fig. 7. The stability limits of the SESAM laser as the cavity GDD β'' varies. Here, the lines (C_s, upper) and S_s, as previously defined in Fig. 2, are the stability limit for the continuous waves and the wake modes, respectively.

5. Conclusion

In summary, we have studied how the parameters of the slow saturable absorption (SSA) affect the performance of a soliton fiber comb laser. As the recovery time T_A decreases from picoseconds to sub-picoseconds, the modelocking can be destablized by different mechanisms. In general, as T_A decreases, the absorption recovery occurs more quickly while the absorption depth decreases. No modelocking exists as T_A approaches zero as the absorption depth becomes too small to support a modelocked pulse. Saturable absorbers with small non-zero values of T_A behave similarly to a fast saturable absorber with a small saturation depth, in which case the modelocking can be destabilized by continuous waves. When T_A grows, the wake modes instability appears as cavity gain increases. Wake modes appear in the net gain window that is formed by the slow recovery of the absorption and the even-slower saturable gain, destabilizing the modelocked pulse.

Optics EXPRESS

In this article, we described two approaches that can help suppress the wake modes and stabilize the modelocking. Smaller values of saturation energy saturate the absorption more easily, leading to deeper and narrower net gain windows. In addition, large values of negative group-delay dispersion (GDD) helps suppress the wake modes and stabilize the modelocking by sweeping the growing modes out of the gain window [35].

Based on this dynamical stability structure, we show that significantly larger output power and bandwidth can be achieved by selecting a SSA with carefully selected parameters. In particular, the largest cavity gain is the key factor enabling more energetic modelocked pulses with a broader bandwidth. For the laser parameters that we consider here, the cavity gain can be significantly increased when the recovery time is reduced from 2 ps to 0.43 ps, which leads to more than doubling the laser's output energy and bandwidth. This output can be even further improved by introducing a more negative GDD and a lower saturation energy for the SESAM. Previous results [49] have shown that higher output coupling ratios can further increase the pulse energy and bandwidth without sacrificing the noise performance. Combining all these results, we can predict that many SSA-based fiber comb lasers can be optimized to support significantly higher power comb outputs with a broader bandwidth.

In this artile, our optimization goal is to increase the laser's output power and bandwidth by varying the SSA's recovery time T_A and saturation energy w_A, as well as the group delay dispersion. Here, based on our prior optimization efforts [35,43,49,50], we provide a brief summary to our prior results in Table 2. For future work, we plan to conduct a more exhaustive optimization effort in the laser's adjustable parameters, which might include fiber parameters, the saturation parameters, as well as the cavity designs structures. In addition, we also plan to include lowering the comb lasers' noise, including the carrier envelope phase noise [51] and the timing jitter phase noise [52], as a key optimization goal.

Table 2. To optimize the output parameters of a soliton comb laser, the preferred variation of the parameters of the laser cavity.

Parameter	Perferred variation	Notes
g_0	larger	Achieving higher values of g_0 is the key to optimize the soliton comb lasers' output parameters. Larger values of g_0 is achieved by increasing pump power.
β''	more negative	Larger values of negative GDD can help avoid the most unstable perturbations: the wake modes [35].
w_A	smaller	See an example in Fig. 5. Smaller values of w_A can be achieved with smaller saturation fluence.
t_{out}	larger	Larger output coupling ratios can allow higher values of g_0 without triggering the wake mode instability while increasing the power efficiency [49,50].
T_A	from 0.2 ps to 0.5 ps	In this work, optimal values of T_A are from 0.2 ps to 0.5 ps, where smaller values of w_A and more negative values of β'' leads to smaller optimal values of T_A. In general, the optimal value of T_A depends on the specific values of w_A, β'', and t_{out}.

Here, our work focuses on a generic model for slow saturable absorbers, Eq. (5), without considering the manufacturing details. In practical designs, availability of cavity components can also pose limits on which SESAM to choose. In addition, it has been reported that two-photon absorption can lead to inaccurate evaluations of the SESAM's absorption curves, especially in GaAs-based SESAMs [53,54] with high fluences. While particular model inaccuracy should not affect our results since we focus on SESAMs with lower values of w_A, as described in Sec. 4, it might affect other designs. These issues will have to be tackled in future work.

Funding. National Natural Science Foundation of China (62075188); Zhejiang Provincial Natural Science Foundation of China (LY21F050007); National Science Foundation (000511-00001).

Optics EXPRESS

Disclosures. The authors declare no conflicts of interest.

Data availability. Data underlying the results presented in this paper are not publicly available at this time but may be obtained from the authors upon reasonable request.

References

1. J. L. Hall, "Nobel lecture: Defining and measuring optical frequencies," Rev. Mod. Phys. **78**(4), 1279–1295 (2006).
2. S. A. Diddams, "The evolving optical frequency comb [invited]," J. Opt. Soc. Am. B **27**(11), B51–B62 (2010).
3. T. Fortier and E. Baumann, "20 years of developments in optical frequency comb technology and applications," Commun. Phys. **2**(1), 153 (2019).
4. S. A. Diddams, K. Vahala, and T. Udem, "Optical frequency combs: Coherently uniting the electromagnetic spectrum," Science **369**(6501), 1 (2020).
5. N. R. Newbury, "Searching for applications with a fine-tooth comb," Nat. Photonics **5**(4), 186–188 (2011).
6. Z. Kang, C. Mei, L. Zhang, Z. Zhang, J. Evans, Y. Cheng, K. Zhu, X. Zhang, D. Huang, Y. Li, J. He, Q. Wu, B. Yan, K. Wang, X. Zhou, K. Long, F. Li, Q. Li, S. Wang, J. Yuan, P. Wai, and S. He, "Advanced progress on $\chi^{(3)}$ nonlinearity in chip-scale photonic platforms (invited review)," Prog. Electromagn. Res. **170**, 17–62 (2021).
7. H. A. Haus, "Mode-locking of lasers," IEEE J. Sel. Top. Quant. **6**(6), 1173–1185 (2000).
8. L. C. Sinclair, I. Coddington, W. C. Swann, G. B. Rieker, A. Hati, K. Iwakuni, and N. R. Newbury, "Operation of an optically coherent frequency comb outside the metrology lab," Opt. Express **22**(6), 6996–7006 (2014).
9. L. Nelson, D. Jones, K. Tamura, H. Haus, and E. Ippen, "Ultrashort-pulse fiber ring lasers," Appl. Phys. B **65**(2), 277–294 (1997).
10. B. R. Washburn, R. W. Fox, N. R. Newbury, J. W. Nicholson, K. Feder, P. S. Westbrook, and C. G. Jørgensen, "Fiber-laser-based frequency comb with a tunable repetition rate," Opt. Express **12**(20), 4999–5004 (2004).
11. C.-J. Chen, P. K. A. Wai, and C. R. Menyuk, "Soliton fiber ring laser," Opt. Lett. **17**(6), 417–419 (1992).
12. S. Droste, G. Ycas, B. R. Washburn, I. Coddington, and N. R. Newbury, "Optical frequency comb generation based on erbium fiber lasers," Nanophotonics **5**(2), 196–213 (2016).
13. T. R. Schibli, K. Minoshima, F.-L. Hong, H. Inaba, A. Onae, H. Matsumoto, I. Hartl, and M. E. Fermann, "Frequency metrology with a turnkey all-fiber system," Opt. Lett. **29**(21), 2467–2469 (2004).
14. H. Byun, M. Y. Sander, A. Motamedi, H. Shen, G. S. Petrich, L. A. Kolodziejski, E. P. Ippen, and F. X. Kärtner, "Compact, stable 1 GHz femtosecond Er-doped fiber lasers," Appl. Opt. **49**(29), 5577–5582 (2010).
15. M. C. Stumpf, S. Pekarek, A. E. H. Oehler, T. Südmeyer, J. M. Dudley, and U. Keller, "Self-referencable frequency comb from a 170-fs, 1.5-μm solid-state laser oscillator," Appl. Phys. B **99**(3), 401–408 (2010).
16. C. Kim, K. Jung, K. Kieu, and J. Kim, "Low timing jitter and intensity noise from a soliton Er-fiber laser mode-locked by a fiber taper carbon nanotube saturable absorber," Opt. Express **20**(28), 29524–29530 (2012).
17. P. Langlois, M. Joschko, E. R. Thoen, E. M. Koontz, F. X. Kärtner, E. P. Ippen, and L. A. Kolodziejski, "High fluence ultrafast dynamics of semiconductor saturable absorber mirrors," Appl. Phys. Lett. **75**(24), 3841–3843 (1999).
18. U. Keller, "Ultrafast solid-state laser oscillators: a success story for the last 20 years with no end in sight," Appl. Phys. B **100**(1), 15–28 (2010).
19. "SAM—saturable absorber mirror," https://www.batop.de/information/SAM_infos.html. Accessed: 2021-08-16.
20. D. Popa, Z. Sun, T. Hasan, W. B. Cho, F. Wang, F. Torrisi, and A. C. Ferrari, "74-fs nanotube-mode-locked fiber laser," Appl. Phys. Lett. **101**(15), 153107 (2012).
21. S. Set, H. Yaguchi, Y. Tanaka, and M. Jablonski, "Laser mode locking using a saturable absorber incorporating carbon nanotubes," J. Lightwave Technol. **22**(1), 51–56 (2004).
22. Y.-W. Song, S. Yamashita, C. S. Goh, and S. Y. Set, "Carbon nanotube mode lockers with enhanced nonlinearity via evanescent field interaction in d-shaped fibers," Opt. Lett. **32**(2), 148–150 (2007).
23. D. Kim, N. H. Park, H. Lee, J. Lee, D.-I. Yeom, and J. Kim, "Graphene-based saturable absorber and mode-locked laser behaviors under gamma-ray radiation," Photonics Res. **7**(7), 742–747 (2019).
24. G. Wang, G. Liang, A. A. Baker-Murray, K. Wang, J. J. Wang, X. Zhang, D. Bennett, J.-T. Luo, J. Wang, P. Fan, and W. J. Blau, "Nonlinear optical performance of few-layer molybdenum diselenide as a slow-saturable absorber," Photonics Res. **6**(7), 674–680 (2018).
25. J. Lee, S. Kwon, and J. H. Lee, "Numerical investigation of the impact of the saturable absorber recovery time on the mode-locking performance of fiber lasers," J. Lightwave Technol. **38**(15), 4124–4132 (2020).
26. R. Paschotta and U. Keller, "Passive mode locking with slow saturable absorbers," Appl. Phys. B **73**(7), 653–662 (2001).
27. H. Byun, D. Pudo, J. Chen, E. P. Ippen, and F. X. Kärtner, "High-repetition-rate, 491 mhz, femtosecond fiber laser with low timing jitter," Opt. Lett. **33**(19), 2221–2223 (2008).
28. F. X. Kärtner, J. A. der Au, and U. Keller, "Mode-locking with slow and fast saturable absorbers—what's the difference?" IEEE J. Sel. Top. Quantum Electron. **4**(2), 159–168 (1998).
29. C. J. Saraceno, C. Schriber, M. Mangold, M. Hoffmann, O. H. Heckl, C. R. E. Baer, M. Golling, T. Südmeyer, and U. Keller, "SESAMs for high-power oscillators: Design guidelines and damage thresholds," IEEE J. Sel. Top. Quantum Electron. **18**(1), 29–41 (2012).
30. A. Barh, J. Heidrich, B. O. Alaydin, M. Gaulke, M. Golling, C. R. Phillips, and U. Keller, "Watt-level and sub-100-fs self-starting mode-locked 2.4-μm Cr:ZnS oscillator enabled by GaSb-SESAMs," Opt. Express **29**(4), 5934–5946 (2021).

Optics EXPRESS

31. G. Agrawal, *Nonlinear Fiber Optics*, Optics and Photonics (Elsevier Science, 2010).
32. S. Wang, A. Docherty, B. S. Marks, and C. R. Menyuk, "Comparison of numerical methods for modeling laser mode locking with saturable gain," J. Opt. Soc. Am. B **30**(11), 3064–3074 (2013).
33. O. V. Sinkin, R. Holzlöhner, J. Zweck, and C. R. Menyuk, "Optimization of the split-step fourier method in modeling optical-fiber communications systems," J. Lightwave Technol. **21**(1), 61–68 (2003).
34. C. R. Menyuk and S. Wang, "Spectral methods for determining the stability and noise performance of passively modelocked lasers," Nanophotonics **5**(2), 332–350 (2016).
35. S. Wang, S. Droste, L. C. Sinclair, I. Coddington, N. R. Newbury, T. F. Carruthers, and C. R. Menyuk, "Wake mode sidebands and instability in mode-locked lasers with slow saturable absorbers," Opt. Lett. **42**(12), 2362–2365 (2017).
36. S. Wang, A. Docherty, B. S. Marks, and C. R. Menyuk, "Boundary tracking algorithms for determining the stability of mode-locked pulses," J. Opt. Soc. Am. B **31**(11), 2914–2930 (2014).
37. F. Kärtner, I. Jung, and U. Keller, "Soliton mode-locking with saturable absorbers," IEEE J. Sel. Top. Quantum Electron. **2**(3), 540–556 (1996).
38. H. A. Haus, "Theory of mode locking with a fast saturable absorber," J. Appl. Phys. **46**(7), 3049–3058 (1975).
39. S. Wang, B. S. Marks, and C. R. Menyuk, "Comparison of models of fast saturable absorption in passively modelocked lasers," Opt. Express **24**(18), 20228–20244 (2016).
40. N. N. Akhmediev and A. Ankiewicz, *Dissipative Solitons*, Lecture Notes in Physics (Springer, 2005).
41. T. Kapitula, J. N. Kutz, and B. Sandstede, "Stability of pulses in the master mode-locking equation," J. Opt. Soc. Am. B **19**(4), 740–746 (2002).
42. N. R. Newbury and W. C. Swann, "Low-noise fiber-laser frequency combs (invited)," J. Opt. Soc. Am. B **24**(8), 1756–1770 (2007).
43. S. Wang, T. F. Carruthers, and C. R. Menyuk, "Efficiently modeling the noise performance of short-pulse lasers with a computational implementation of dynamical methods," J. Opt. Soc. Am. B **35**(10), 2521–2531 (2018).
44. "SAM^{TM} data sheet SAM-1550-21-2ps-x, λ = 1550 nm," http://www.batop.com/products/saturable-absorber/saturable-absorber-mirror/saturable-absorber-mirror-1550nm.html. Accessed: 2017-01-14.
45. F. X. Kärtner and U. Keller, "Stabilization of solitonlike pulses with a slow saturable absorber," Opt. Lett. **20**(1), 16–18 (1995).
46. H. Haus and A. Mecozzi, "Noise of mode-locked lasers," IEEE J. Quantum Electron. **29**(3), 983–996 (1993).
47. D. J. Kaup, "Perturbation theory for solitons in optical fibers," Phys. Rev. A **42**(9), 5689–5694 (1990).
48. W. H. Renninger, A. Chong, and F. W. Wise, "Area theorem and energy quantization for dissipative optical solitons," J. Opt. Soc. Am. B **27**(10), 1978–1982 (2010).
49. S. Wang, C. Tu, S. E. J. Mahabadi, S. Droste, L. C. Sinclair, I. Coddington, N. R. Newbury, T. F. Carruthers, and C. R. Menyuk, "Obtaining more energetic modelocked pulses from a sesam-based fiber laser," Opt. Express **28**(14), 20345–20361 (2020).
50. S. Wang, C. R. Menyuk, S. Droste, L. Sinclair, I. Coddington, and N. Newbury, "Optimizing the power efficiency of a sesam fiber comb laser," in *Conference on Lasers and Electro-Optics*, (Optica Publishing Group, 2017), p. SF1C.2.
51. F. Helbing, G. Steinmeyer, and U. Keller, "Carrier-envelope offset phase-locking with attosecond timing jitter," IEEE J. Sel. Top. Quantum Electron. **9**(4), 1030–1040 (2003).
52. R. Paschotta, "Noise of mode-locked lasers (part i): numerical model," Appl. Phys. B **79**(2), 153–162 (2004).
53. A. Saïssy, A. Azema, J. Botineau, and F. Gires, "Absolute measurement of the 1.06 μm two-photon absorption coefficient in GaAs," Appl. Phys. **15**(1), 99–102 (1978).
54. G. H. Jang, J. H. Kim, and T. H. Yoon, "Highly-stable Yb-doped fiber laser mode-locked in a regime of SESAM two-photon absorption," in *CLEO:2011 - Laser Applications to Photonic Applications*, (Optical Society of America, 2011), p. JWA24.